Mathematical and Computational Applications

MDPI

Article

A Network-Based Study of the Dynamics of $A\beta$ and τ Proteins in Alzheimer's Disease

Stefano Bianchi [1,†], Germana Landi [1,*,†], Camilla Marella [2,†], Maria Carla Tesi [1,†], Claudia Testa [2,†] and on behalf of the Alzheimer's Disease Neuroimaging [‡]

[1] Department of Mathematics, University of Bologna, 40126 Bologna, Italy; stefano.bianchi22@unibo.it (S.B.); mariacarla.tesi@unibo.it (M.C.T.)
[2] Department of Physics and Astronomy "Augusto Righi", University of Bologna, 40126 Bologna, Italy; camilla.marella2@unibo.it (C.M.); claudia.testa@unibo.it (C.T.)
* Correspondence: germana.landi@unibo.it
† These authors contributed equally to this work.
‡ Data used in preparation of this article were obtained from the Alzheimer's Disease Neuroimaging Initiative (ADNI) database (adni.loni.usc.edu). As such, the investigators within the ADNI contributed to the design and implementation of ADNI and/or provided data but did not participate in analysis or writing of this report. A complete listing of ADNI investigators can be found at: http://adni.loni.usc.edu/wp-content/uploads/how_to_apply/ADNI_Acknowledgement_List.pdf.

Abstract: Due to the extreme complexity of Alzheimer's disease (AD), the etiology of which is not yet known, and for which there are no known effective treatments, mathematical modeling can be very useful. Indeed, mathematical models, if deemed reliable, can be used to test medical hypotheses that could be difficult to verify directly. In this context, it is important to understand how $A\beta$ and τ proteins, which, in abnormal aggregate conformations, are hallmarks of the disease, interact and spread. We are particularly interested, in this paper, in studying the spreading of misfolded τ. To this end, we present four different mathematical models, all on networks on which the protein evolves. The models differ in both the choice of network and diffusion operator. Through comparison with clinical data on τ concentration, which we carefully obtained with multimodal analysis techniques, we show that some models are more adequate than others to simulate the dynamics of the protein. This type of study may suggest that, when it comes to modeling certain pathologies, the choice of the mathematical setting must be made with great care if comparison with clinical data is considered decisive.

Keywords: Alzheimer's disease; models on graphs; $A\beta$ and τ proteins; medical imaging; numerical simulations

Citation: Bianchi, S.; Landi, G.; Marella, C.; Tesi, M.C.; Testa, C.; on behalf of the Alzheimer's Disease Neuroimaging. A Network-Based Study of the Dynamics of $A\beta$ and τ Proteins in Alzheimer's Disease. *Math. Comput. Appl.* **2024**, *29*, 113. https://doi.org/10.3390/mca29060113

Academic Editor: Sundeep Singh

Received: 10 October 2024
Revised: 15 November 2024
Accepted: 25 November 2024
Published: 4 December 2024

1. Introduction

Alzheimer's disease (AD) is a neurodegenerative disorder characterized by a progressive decline in memory and other cognitive functions, leading inevitably to death. It is an incurable disease affecting more than 50 million people, with figures set to increase significantly in the coming years (World Alzheimer Report 2023). The etiology of the disease is unclear to date, but two proteins are universally recognized as playing a crucial role in the development of the disease: amyloid-beta $(A\beta)$ and tau (τ). Both proteins are physiologically present in the brain but, in the presence of the disease, they form abnormal aggregates, in a progressive and irreversible way. Indeed, $A\beta$ plaques and neurofibrillary tangles (NFTs) of τ are pathological hallmarks of AD. Experimental studies suggest non-uniform distributions of pathological proteins in the brain [1]. Both $A\beta$ and τ exhibit characteristic spatiotemporal deposition patterns. NFTs appear first in the entorhinal cortex and then spread to the amygdala, temporal areas, and, finally, throughout the cortex [2]. On the other hand, $A\beta$ plaques form first in the temporal and frontal areas and then spread to other areas of the brain [2,3]. Recent literature suggests that the interplay between the two

proteins should be crucial in the development of the disease and must be taken into account for the development of new therapies [4–6]. Clearly, when one is interested in modeling complex pathologies such as AD, comparison with clinical and experimental data is crucial to the reliability of the study. Clinical multimodal neuroimages, if properly processed in terms of harmonization, combination, and a quantitative approach, can give information of local character, providing, for instance, the concentration of proteins in different brain regions [7].

This work has two main objectives. One is to capture such types of non-uniform distributions through appropriate mathematical models. The other purpose is to compare the results from the mathematical models with clinical data in the context of Alzheimer's disease. Comparison with clinical data is a fundamental step in the development of a trustable mathematical model but it is rarely addressed in the mathematical modeling literature. To this aim, we have processed a considerable amount of clinical neuroimages to extract quantitative features, which can be compared with the τ concentration values provided by the mathematical models.

Networks are mathematical tools that provide an ideal setting for comparisons between clinical data and numerical results from models. Complex network properties have been identified with some consistency in all modalities of neuroimaging data and over a range of spatial and time scales. Thus, brain networks allow to describe the information process in neurons and its characteristics of being both locally specialized or segregated and globally distributed or integrated [8]. In particular, small-worldness characterizes an intermediate regime of networks between the two extreme regimes of a regular lattice and a random network, efficiently representing the brain structure [9]. The mathematical modeling of AD can be very useful for integrating clinical and experimental data in a theoretical setting, which could allow, once reliability has been verified, to test various hypotheses otherwise difficult to verify. For an exhaustive overview of existing mathematical models of proteins spreading on networks and of various related challenging questions, we refer to [10]. Here, we wish to emphasize that the dynamics of the two proteins we are interested in differ in several respects, both spatial ($A\beta$ spreads over small distances, τ over large distances) and temporal (the dynamics of $A\beta$ are much faster than those of τ). Differences in spatial dynamics should, in some way, be reflected by the choice of network used for the evolution of the dynamics. This paper is inspired by the paper [11] as far as the idea of using distinct networks for different protein dynamics is concerned; however, its purpose is quite different. Indeed, in [11], the authors were mainly interested in investigating the synergistic interactions of the two proteins $A\beta$ and τ, whose relevance was confirmed there by testing various modeling hypotheses. However, the authors were not interested in any comparison with medical data. Here, we strongly rely on the comparison with medical data to test different modeling hypotheses concerning the diffusion of τ on properly chosen networks, to see if there is an optimal way to deal with the spreading of proteins when it comes to modeling AD. Therefore, the main target of this paper is twofold: 1. to consider different models for the spreading of $A\beta$ and, especially, of τ, developed on networks with a precise biomedical meaning; 2. to have medical data for a comparison as meaningful as possible with the models, and to use that comparison to test the trustability of the model.

The plan of the work is the following: in Section 2, we describe the networks we use for our models. We start from publicly available data and, from that, we construct several different weighted graphs on which we evolve proteins. In Section 3, we describe the models we study; in particular, we present four different models for various possible mechanisms of the spreading of τ. Section 4 is concerned with the procedures we have adopted to obtain reliable medical data. We emphasize that we used a multimodal approach, based on MRI and PET, to determine the concentrations of τ protein in the brain. Finally, in Section 5, we present the results obtained by numerical simulations and we make comparisons with medical data.

2. Brain Networks via Weighted Graphs

The central concept of a brain network constructed to segregate and integrate information processing comes from the advent of the "disconnection syndromes" hypothesis [12], mainly on the basis of clinico-pathological correlations. The conceptualization of the relationship between the structure and function of the brain has led to understand that brain regions participate in many functions, introducing the structure–function framework described by a network of brain regions. Mesulam and colleagues [13] introduced the network approach to understand the localization of complex functions. The connection matrix of the human brain, known as the human "connectome", today represents an indispensable tool for mapping brain structure to functional processes and has a valuable impact on understanding brain diseases.

To model the spreading of different proteins in the brain, we consider several connectomes, each corresponding to a different undirected weighted graph. Data used for the construction of these connectomes have been downloaded from the website https://braingraph.org (accessed on 24 November 2024) and consist of an *averaged* graph of 477 healthy subjects, each with 1015 nodes (the weight calculation mode was set as median and the number of fibers launched was set to 20) [14,15]. We stress that the vertices of such a graph do not have associated coordinates that determine their position in space, since it is precisely an averaged graph. This will have consequences when we talk about "distances", which must be understood in an intrinsic sense and not in the classical Euclidean metric sense.

In the following, we first recall the definition of a weighted graph and how to construct an associated Laplacian, mimicking diffusion on it. Then, we describe the weighted graphs we will use to model the spreading of $A\beta$ and τ proteins. A *graph* is a pair $\mathcal{G} = (V, E)$, where V is a set of vertices and $E \subset V \times V$ is a set of the edges; $\mathcal{G}$ is said to be undirected if $(i, j) \in E$ implies that $(j, i) \in E$. The graph $\mathcal{G}$ is called weighted if a measure $\omega : E \to \mathbb{R}^+$ exists, assigning a unique positive number to each edge; the value $\omega(i, j)$ is referred to as the weight of the edge (i, j). A weighted graph can be represented through the adjacency matrix A whose entries $A_{i,j}$ represent the weights of the edge (i, j). Let $N = |V|$ be the number of vertices in $\mathcal{G}$; then, $A \in \mathbb{R}^{N\times N}$ is defined as

$$A_{i,j} = \begin{cases} w(i,j) & \text{if } (i,j) \in E; \\ 0 & \text{otherwise.} \end{cases}$$

There are several possible definitions for the Laplacian associated with a given graph. Given the adjacency matrix $A \in \mathbb{R}^{N\times N}$ of $\mathcal{G}$, following [16], we define the graph Laplacian L as $L = D - A$ where D is the weighted degree matrix whose jth diagonal element $D_{j,j}$ is given by

$$D_{j,j} = \sum_{i=1}^{N} A_{i,j}.$$

2.1. Structural Connectome

We call *structural connectome* a weighted graph $\mathcal{G} = (V, E)$ extracted from the tractography of diffusion tensor images of 477 healthy subjects of the Human Connectome Project [17] using the Budapest Reference Connectome v3.0 [15]. In this graph, vertices correspond to parcellated regions of gray matter formed by neurons, which share similarities in cytoarchitecture, functional activity, and structural connections to other regions, and edges represent the connectivity between the regions. We used a high-resolution connectome with $N = 1015$, which can be downloaded at the website https://pitgroup.org/connectome/ (accessed on 24 November 2024). It is possible to choose, for the edges of this graph,

different weights, based on the mean number of fibers connecting two regions, and on their mean length. Accordingly, we denote by $\mathcal{G}_{\mathrm{NL}}$ the graph with weights given by

$$w_{\mathrm{NL}}(i,j) = \frac{n_{ij}}{\ell_{ij}}, \tag{1}$$

where n_{ij} is the mean number of fibers connecting vertices i and j, and ℓ_{ij} is the mean length of such fibers. Analogously, we denote by $\mathcal{G}_{\mathrm{L}}$ the graph with weights given by

$$w_{\mathrm{L}}(i,j) = \ell_{ij}. \tag{2}$$

Therefore, the two weighted graphs $\mathcal{G}_{\mathrm{NL}}$ and $\mathcal{G}_{\mathrm{L}}$ have the same vertices and edges, but different weights.

2.2. Intrinsic Proximity Connectome

Let $R_{\mathrm{P}} \in \mathbb{R}^+$ be a given positive value; the *intrinsic proximity connectome* is the weighted graph $\mathcal{G}_{\mathrm{P}} = (V, E)$ whose set of vertices V is the same as $\mathcal{G}_{\mathrm{L}}$'s and whose set of edges $E_{\mathrm{P}} \subset E_{\mathrm{L}}$ is the subset of edges of $\mathcal{G}_{\mathrm{L}}$ connected by a fiber with length ℓ less than R_{P}. The weights are given by

$$w_{\mathrm{P}}(i,j) = \begin{cases} e^{-\ell_{ij}^2/\sigma} & \text{if } \ell_{ij} \le R_{\mathrm{P}} \\ 0 & \text{otherwise,} \end{cases}$$

where $\sigma \in \mathbb{R}^+$ is a fixed parameter. In this way, we connect two vertices only if they are close in an intrinsic sense, as opposed to a "geometric" vicinity measured with some kind of Euclidean distance. Indeed, as already mentioned, the vertices of the graph do not have associated spatial coordinates. The weights we assign are stronger for intrinsically close vertices. For this reason, $\mathcal{G}_{\mathrm{P}}$ is referred to as *intrinsic proximity connectome*. It is appropriate to emphasize here that this proximity connectome is quite different from the one used in [11]. Indeed, here, we use only *intrisic* connections, without adding any new connection, and we give them a weight proportional to the intrinsic distance.

2.3. Cumulative Connectome

The *cumulative connectome* is a weighted graph $\mathcal{G}_{\mathrm{C}} = (V, E)$ with the same V and E as $\mathcal{G}_{\mathrm{NL}}$, but with weights defined as follows. Let $\mathcal{S}_{ij}$ be the set of all paths in the graph $\mathcal{G}_{\mathrm{NL}}$ starting at vertex i and ending at vertex j, i.e.,

$$\mathcal{S}_{ij} = \{p_{ij}^1, p_{ij}^2, \ldots, p_{ij}^{m_{ij}}\}, \tag{3}$$

where $m_{ij} = |\mathcal{S}_{ij}|$ and each path $p_{ij}^k \in \mathcal{S}_{ij}$ consists of a sequence of edges:

$$p_{ij}^k = \{e_{ij}^{k_1}, e_{ij}^{k_2}, \ldots, e_{ij}^{k_r}\}, \quad k = 1, \ldots, m_{ij}.$$

We recall that the graphs $\mathcal{G}_{\mathrm{NL}}$ and $\mathcal{G}_{\mathrm{L}}$ differ only in the weights assigned to the edges; thus, we can define the length of the path p_{ij}^k, considering it as a part of the graph $\mathcal{G}_{\mathrm{L}}$ or the graph $\mathcal{G}_{\mathrm{NL}}$. Since the length of a path is usually defined as the sum of the weights of the edges forming the path, in $\mathcal{G}_{\mathrm{NL}}$, we obtain the length $l_{\mathrm{NL}}(p_{ij}^k)$ defined as

$$l_{\mathrm{NL}}(p_{ij}^k) = \sum_{s \in \{k_1, \ldots, k_r\}} w_{\mathrm{NL}}(e_{ij}^s), \quad k = 1, \ldots, m_{ij},$$

and, in $\mathcal{G}_{\mathrm{L}}$ we obtain the length $l_{\mathrm{L}}(p_{ij}^k)$ given by

$$l_{\mathrm{L}}(p_{ij}^k) = \sum_{s \in \{k_1, \ldots, k_r\}} w_{\mathrm{L}}(e_{ij}^s), \quad k = 1, \ldots, m_{ij}.$$

Finally, let $\mathcal{S}_{ij}^{\delta}$ be the subset of $\mathcal{S}_{ij}$ such that

$$\mathcal{S}_{ij}^{\delta} = \{p_{ij}^{k} \in \mathcal{S}_{ij} \mid l_{\mathrm{L}}(p_{ij}^{k}) \leq \delta\} \tag{4}$$

where $\delta \in \mathbb{R}^{+}$ is a fixed parameter. Two vertices i and j are connected in the cumulative connectome $\mathcal{G}_{\mathrm{C}}$ if there is at least one path of length in $\mathcal{G}_{\mathrm{L}}$ less or equal to δ joining them (we call such a path an admissible path). In the affirmative case, the weight of the edge connecting vertices i and j is given by the sum of the lengths in $\mathcal{G}_{\mathrm{NL}}$ of all admissible paths (hence the name cumulative connectome):

$$w_{\mathrm{C}}(i,j) = \sum_{p_{ij}^{k} \in \mathcal{S}_{ij}^{\delta}} l_{\mathrm{NL}}(p_{ij}^{k}).$$

Summarizing, in the cumulative connectome, two vertices i and j are connected if there is at least one path starting at i and ending at j whose length is smaller than a fixed value δ. Vertices that are not connected in $\mathcal{G}_{\mathrm{NL}}$ are connected in $\mathcal{G}_{\mathrm{C}}$ if there is an admissible path in $\mathcal{G}_{\mathrm{NL}}$ joining them. In this way, we encode in $\mathcal{G}_{\mathrm{C}}$ connections between brain regions over long distances. In other words, we connect two vertices if the corresponding brain regions are joined by axonal paths with a length determined by a δ parameter that we choose. The weights of the connections depend on the number and length of the axonal fibers in the connections.

3. The Models

By choosing appropriate graphs among the ones introduced in the previous section, we set up different models to describe the dynamics of $A\beta$ and τ proteins. The choice of the graphs is guided by the main biological features characterizing the two proteins and their dynamics.

Concerning $A\beta$, it is well known that monomeric $A\beta$ peptides originate physiologically from the cleavage of the transmembrane protein APP (amyloid precursor protein), and are considered non toxic [18]. Then, for a reason not yet clarified, an imbalance between the production and clearance of the protein can occur, giving rise to a process of agglomerations. This leads to the formation of toxic amyloid fibrils [19,20], often referred to as oligomers. These oligomers eventually accumulate in insoluble agglomerates known as senile plaques, nowadays considered non toxic [19]. To describe this process, we adopted a so-called compartmental model, that is, we considered $A\beta$ proteins assuming only three types of conformations: monomers, oligomers (which include all soluble conformations that are not monomers), and plaques (insoluble conformations). Moreover, we wanted to take into account that the $A\beta$ protein diffuses on short distances and its dynamics (production, aggregation, and clearance) are fast [21]. The molar concentration of a protein on the vertices V of a graph are denoted by an N-dimensional vector, where $N = |V|$ is the number of vertices of the graph. Accordingly, the vector-valued functions $\mathbf{u}_j : \mathbb{R} \to \mathbb{R}^N$ describe the molar concentration of $A\beta$ monomers ($j = 1$), oligomers ($j = 2$), and plaques ($j = 3$). We stress that with oligomers we mean aggregates made by two units while with plaques we mean aggregates made by three or more units.

We model $A\beta$ dynamics with the following equations [11]:

$$\begin{cases} \epsilon \dfrac{d\mathbf{u}_1(t)}{dt} = -\gamma_1 L_{\mathrm{P}} \mathbf{u}_1(t) + C_{\mathbf{u}_1} - \alpha \mathbf{u}_1(t) .* \displaystyle\sum_{j=1}^{3} \mathbf{u}_j(t) - \sigma_1 \mathbf{u}_1(t) & \text{(5a)} \\ \epsilon \dfrac{d\mathbf{u}_2(t)}{dt} = -\gamma_2 L_{\mathrm{P}} \mathbf{u}_2(t) + \dfrac{\alpha}{2} \mathbf{u}_1(t) .* \mathbf{u}_1(t) - \alpha \mathbf{u}_2(t) .* \displaystyle\sum_{j=1}^{3} \mathbf{u}_j(t) - \sigma_2 \mathbf{u}_2(t) & \text{(5b)} \\ \epsilon \dfrac{d\mathbf{u}_3(t)}{dt} = \dfrac{\alpha}{2} \displaystyle\sum_{3 \leq j+k < 6} \mathbf{u}_j(t) .* \mathbf{u}_k(t) - \sigma_3 \mathbf{u}_3(t) & \text{(5c)} \end{cases}$$

where $.*$ denotes the element-wise product between vectors. System (5) is endowed with initial conditions at $t = 0$ as follows (at the initial time, the brain is healthy; therefore, only $A\beta$ monomers are present):

$$\begin{cases} \mathbf{u}_1(0) = C_{\mathbf{u}_1}\mathbf{1} \\ \mathbf{u}_2(0) = \mathbf{0} \\ \mathbf{u}_3(0) = \mathbf{0} \end{cases} \tag{6}$$

where $\mathbf{0}$ and $\mathbf{1}$ denote the N-dimensional vectors whose components are all equal to zero and one, respectively. Since t denotes a slow time variable, the ϵ in front of the equations takes into account the fact that the processes described are fast [21]. The first term in Equations (5a) and (5b) models the diffusion of $A\beta$ monomers and oligomers along the network. Since this protein spreads along short distances, we choose the intrinsic proximity connectome to model the network. Indeed, on the intrinsic proximity connectome $\mathcal{G}_{\mathrm{P}}$, two vertices i and j are connected only if the mean length of the axonal fibers connecting the corresponding regions of the brain is sufficiently short; in addition, the shorter the fiber length, the greater the weight of the corresponding edge. Accordingly, here, diffusion is driven by the graph Laplacian L_{P}. In the first equation, the term $C_{\mathbf{u}_1}$ represents a source term (gain) due to the physiological production of $A\beta$ monomers, the term $-\alpha\mathbf{u}_1(t).*\sum_{j=1}^{3}\mathbf{u}_j(t)$ is a loss due to the aggregation of monomers with other $A\beta$ proteins and the term $-\sigma_1\mathbf{u}_1(t)$ is a loss due to clearance phenomena. In the second equation, the term $\frac{\alpha}{2}\mathbf{u}_1(t).*\mathbf{u}_1(t)$ is a gain in oligomers due to the aggregation of two monomers, while the next two terms are losses analogous to those in the first equation. Finally, in the third equation, the diffusion term is absent since plaques are insoluble (they are too heavy to diffuse); there is a gain term due to aggregation (for a detailed explanation of this term and, in general, on the use of Smoluchowki's equations in this context, see [6]) and a loss term due to clearance. We stress that, in the equations governing the dynamics of $A\beta$ proteins, there is no coupling with the τ protein. Indeed, such a coupling will be present in the equation governing the dynamics of τ.

The protein τ is a physiological microtubule-associated protein: its main function is to stabilize microtubules and to regulate axonal transport. In brains affected by AD, misfolded τ has been found in the form of aggregates called neurofibrillary tangles, which, together with $A\beta$ plaques, are a hallmark of AD [22]. Misfolded τ is toxic for the neuron; indeed, it compromises stabilization, transport, and, in general, interferes with neuronal functions. As already mentioned in the Introduction, in recent years, there has been a consensus in the scientific community to consider a synergistic effect of $A\beta$ and τ when it comes to AD [4,23,24]. More precisely, the "trigger and bullet" hypothesis identifies in toxic $A\beta$ peptides the trigger for τ misfolding: the bullet is the misfolded τ, which, in turn, causes neural damage until, eventually, the neuron's death [25–27]. Concerning the spreading mechanism of misfolded τ, it has been proposed that neuronal damage spreads in the neuronal net through a neuron-to-neuron prion-like propagation mechanism [28–31]. Based on the considerations presented so far, the dynamics of misfolded τ, whose concentration is given by the vector-valued function $\mathbf{w} : \mathbb{R} \to \mathbb{R}^N$, are governed by the following equation [11]:

$$\frac{d\mathbf{w}(t)}{dt} = \gamma_3 K[\mathbf{w}] + C_{\mathbf{w}} \cdot \left(\mathbf{u}_2(t) - U_{\mathbf{w}}\right)^+ + s_{\mathbf{w}}(t) - \sigma_4\mathbf{w}(t) \tag{7}$$

endowed with the initial condition (at the initial time, the brain is healthy; therefore, there is no misfolded τ):

$$\mathbf{w}(0) = \mathbf{0}. \tag{8}$$

Here, we see the coupling between $A\beta$ and τ. Indeed, the second term $C_{\mathbf{w}} \cdot \left(\mathbf{u}_2(t) - U_{\mathbf{w}}\right)^+$ in the equation rules the interaction of the two proteins: if $\mathbf{u}_2$, the toxic form of $A\beta$, is above a given threshold, then it triggers the misfolding of τ. The term $s_{\mathbf{w}}(t)$ represents a source of

misfolded τ, typically located in the enthorinal region of the brain [2], while the last term is the loss due to clearance.

The main purpose of this work is to investigate different possible forms for the operator K, appearing as the first term in (7), modeling the spreading of τ. As already mentioned, the spreading of such a protein can take place over long distances [32], possibly following a prion-like type of process [30], on a slow time scale. Several models have appeared in the literature concerning various possible mechanisms of τ spreading on networks [11,33–40]. Here, we considered four different possibilities (corresponding to four different mathematical models) for the operator K, and we made a comparison between the results obtained for each model and clinical data. In this way, we tried to determine if there is one form for K better describing the dynamics we were interested in reproducing. The full system of equations we studied is, therefore, given by

$$\begin{cases} \epsilon \dfrac{d\mathbf{u}_1(t)}{dt} = -\gamma_1 L_{\mathrm{P}} \mathbf{u}_1(t) + C_{\mathbf{u}_1} - \alpha \mathbf{u}_1(t) .* \displaystyle\sum_{j=1}^{3} \mathbf{u}_j(t) - \sigma_1 \mathbf{u}_1(t) & \text{(9a)} \\ \epsilon \dfrac{d\mathbf{u}_2(t)}{dt} = -\gamma_2 L_{\mathrm{P}} \mathbf{u}_2(t) + \dfrac{\alpha}{2} \mathbf{u}_1(t) .* \mathbf{u}_1(t) - \alpha \mathbf{u}_2(t) .* \displaystyle\sum_{j=1}^{3} \mathbf{u}_j(t) - \sigma_2 \mathbf{u}_2(t) & \text{(9b)} \\ \epsilon \dfrac{d\mathbf{u}_3(t)}{dt} = \dfrac{\alpha}{2} \displaystyle\sum_{3 \le j+k < 6} \mathbf{u}_j(t) .* \mathbf{u}_k(t) - \sigma_3 \mathbf{u}_3(t) & \text{(9c)} \\ \dfrac{d\mathbf{w}(t)}{dt} = \gamma_3 K[\mathbf{w}] + C_{\mathbf{w}} \cdot \left(\mathbf{u}_2(t) - U_{\mathbf{w}}\right)^{+} + s_{\mathbf{w}}(t) - \sigma_4 \mathbf{w}(t) & \text{(9d)} \end{cases}$$

3.1. Model 1: Diffusion of τ Along the Structural Connectome $\mathcal{G}_{\mathrm{NL}}$

Following previous works in the literature [6,11,33,38], a quite standard choice to model the spreading of τ protein along edges of a connectome consists of choosing the Laplacian L_{NL} associated with the structural connectome $\mathcal{G}_{\mathrm{NL}}$. In this way, spreading corresponds to diffusion and we have

$$K[\mathbf{w}] = -L_{\mathrm{NL}} \mathbf{w}. \tag{10}$$

3.2. Model 2: Diffusion of τ Along the Cumulative Connectome $\mathcal{G}_{\mathrm{C}}$

In the cumulative connectome, two vertices are connected if there exists at least one admissible path between them. Such a path can be formed by several consecutive edges, each with its own weight contributing to the final weight. The corresponding Laplacian L_{C} therefore encodes the structure of the brain with connections spanning long distances. For this reason, we choose

$$K[\mathbf{w}] = -L_{\mathrm{C}} \mathbf{w}. \tag{11}$$

We stress again that all distances mentioned in the paper are to be understood not in a geometric but in an intrinsic sense, i.e., referring to fiber lengths, that is, edges, in the graph.

3.3. Model 3: Spreading of τ via Convolution on $\mathcal{G}_{\mathrm{L}}$

A common way of dealing with dynamics occurring over long distances is to make use of integral operators, typically convolutions with an appropriate kernel taking into account distances. With a notation similar to (4), let $\mathcal{S}_{ij}^{\widetilde{\delta}}$ be the subset of $\mathcal{S}_{ij}$ containing all the paths in $\mathcal{G}_{\mathrm{L}}$ from node i to node j with a length less than $\widetilde{\delta}$:

$$\mathcal{S}_{ij}^{\widetilde{\delta}} = \{ p_{ij}^k \in \mathcal{S}_{ij} \mid l_{\mathrm{L}}(p_{ij}^k) \le \widetilde{\delta} \} \tag{12}$$

where $\widetilde{\delta} \in \mathbb{R}^+$ is a fixed parameter. We define the signal k_i on each node i of the graph $\mathcal{G}_{\mathrm{L}}$ as follows:

$$k_i = \sum_{p_{ij}^k \in \mathcal{S}_{ij}^{\widetilde{\delta}}} l_{\mathrm{L}}(p_{ij}^k). \tag{13}$$

Intuitively, k_i accounts for all the paths between i and each vertex j in $\mathcal{G}_{\mathrm{L}}$ that is not too far from i and plays the role of the convolution kernel. The convolution product on $\mathcal{G}_{\mathrm{L}}$ between $\mathbf{k}$ and $\mathbf{w}$ is defined by using the graph Laplacian eigenvectors [41]. Let $\{\mathbf{v}_\ell\}_{\ell=1,\dots,N}$ be a complete set of orthonormal eigenvectors of the Laplacian L_{L} of $\mathcal{G}_{\mathrm{L}}$ with eigenvalues $\{\lambda_\ell\}_{\ell=1,\dots,N}$ ordered in nondecreasing order and let $U \in \mathbb{R}^{N\times N}$ be the matrix whose columns correspond to the eigenvectors $\mathbf{v}_\ell$, $\ell = 1,\dots,N$. The graph Fourier transform $\hat{\mathbf{k}}$ of the signal $\mathbf{k}$ on $\mathcal{G}_{\mathrm{L}}$ is defined as the expansion of $\mathbf{k}$ in terms of the eigenvectors of L_{L}, i.e.,

$$\hat{\mathbf{k}} = U^*\mathbf{k} \tag{14}$$

where * denotes the conjugate transpose of a matrix. The inverse graph Fourier transform is given by

$$\mathbf{k} = U\hat{\mathbf{k}}. \tag{15}$$

The convolution product on $\mathcal{G}_{\mathrm{L}}$ between $\mathbf{k}$ and $\mathbf{w}$ is the vector $\mathbf{k} * \mathbf{w}$ such that

$$\mathbf{k} * \mathbf{w} = U(\hat{\mathbf{k}}. * \hat{\mathbf{w}}) \tag{16}$$

where $\hat{\mathbf{w}}$ is the graph Fourier transform of $\mathbf{w}$ defined as in (14). We choose $K[\mathbf{w}]$ as the convolution product of $\mathbf{w}$ with $\mathbf{k}$:

$$K[\mathbf{w}] = \mathbf{k} * \mathbf{w}. \tag{17}$$

3.4. Model 4: Spreading of τ via Convolution on $\mathcal{G}_{\mathrm{NL}}$

In [36,37], the authors introduce a graph convolution operator as a nonlocal model for the conversion from a healthy protein to a toxic one. Inspired by these works, we use their nonlocal operator to model the prion-like spreading of misfolded τ proteins. Let $M \in \mathbb{R}^{N\times N}$ be the matrix whose elements $m_{i,j}$, $i,j = 1,\dots,N$, are the length of the shortest path from vertex i to vertex j in the graph $\mathcal{G}_{\mathrm{NL}}$. If two vertices are not connected, $m_{i,j} = 0$. Moreover, let $\widetilde{M} \in \mathbb{R}^{N\times N}$ be the matrix with elements

$$\widetilde{m}_{i,j} = e^{-\eta^2 m_{i,j}^2}, \quad i,j = 1,\dots,N, \tag{18}$$

where η is a positive parameter. Finally, let $C \in \mathbb{R}^{N\times N}$ be the matrix defined as

$$c_{i,j} = \frac{\widetilde{m}_{i,j}}{\sum_{k=1}^{N} \widetilde{m}_{i,k}}, \quad i,j = 1,\dots,N. \tag{19}$$

Then, the operator $K[\mathbf{w}]$ is chosen as

$$K[\mathbf{w}] = C\mathbf{w}. \tag{20}$$

4. Methods

4.1. Data Availability

Data used in the preparation of this article were obtained from the ADNI Initiative (ADNI) database (https://adni.loni.usc.edu/, accessed on 24 November 2024). As described on the ADNI website, ADNI was launched in 2003 as a public–private partnership, led by Principal Investigator Michael W. Weiner, MD. The primary goal of ADNI has been to test whether serial MRI, positron emission tomography (PET), other biological markers, and clinical and neuropsychological assessments can be combined to measure

the progression of mild cognitive impairment (MCI) and early Alzheimer's disease. For up-to-date information, see www.adni-info.org (accessed on 24 November 2024).

4.2. Subjects

The study included a total of 261 participants: 238 Cognitive Normal (CN) subjects (mean age $\pm$ *st.dev.* $= 72.7y \pm 8.7y$; M:F = 86:152), and 23 AD (mean age $\pm$ *st.dev.* $= 73.1y \pm 9.6y$; M:F = 11:12) from the Alzheimer's Disease Neuroimaging Initiative (ADNI). All data were downloaded from ADNI3. The number of included subjects is the consequence of the following inclusion criteria. To quantitatively measure the concentration of τ in the brain regions, we considered subjects having undergone a PET imaging with the radiotracer [^{18}F]-AV1451 and a corresponding accelerated sagittal T1-weighted anatomical image acquired using a 3D magnetization-prepared rapid acquisition gradient echo (MPRAGE) sequence from Siemens 3T MRI scanners to minimize effects of inter-scanner variability. To eliminate the known variability of the results due to the radiopharmaceutical used, we only considered PET images obtained with the same radiopharmaceutical ([^{18}F]-AV151). Moreover, we decided to select MR scan obtained only by 3T scanners produced by a single vendor, again to reduce variability. PET and MRI imaging were chosen to be acquired at no more than 3 months of temporal distance from one another. This substantial limitation was applied to prevent different image modalities from reflecting a different pathological condition of the same subject due to the progression of dementia.

4.3. PET Acquisition and Processing

[^{18}F]-AV1451 imaging acquisition and pre-processing in ADNI3 consisted of the baseline [^{18}F]-AV1451 PET scan (first scan acquired) for each subject, injection of 370 MBq (10 mCi) of tracer, and a 30 min dynamic scan consisting of six 5 min frames 75 min post-injection. Pre-processing consisted of the co-registration of separated frames to minimize patient motion effect, average of the 5 frames to obtain a single 30 min PET scan, re-orienting to a standardized space and normalization of intensity, and, finally, the application of a filter specific for the type of scanner.

4.4. MRI Structural Imaging Acquisition and Processing

The MRI structural images chosen within 3 months to the date of [^{18}F]-AV151 PET, were pre-processed, segmented, and parcellated with FreeSurfer 6.0 (http://surfer.nmr.mgh.harvard.edu/, accessed on 24 November 2024), in order to subdivide the brain volumes into a set of 83 anatomical cortical and subcortical region of interest (ROIs), separated between left and right hemisphere (with the addition of the brain stem) and belonging to six main networks within the brain: the frontal, the parietal, the occipital, the temporal, and the limbic lobes, plus the basal ganglia [42,43]. The subdivision just described was also chosen based on the prior hypothesis that the limbic system is specially affected by the disease. A complete list of the regions, the abbreviation of their names, and the network they belong to can be seen in the Appendix A. Nodes of the brain graphs were put in correspondence with the 83 ROIs, considering the anatomical information of each vertex, to compare τ concentrations relative to the 83 ROIs in the PET images and the concentrations estimated by the mathematical models.

4.5. PET and MRI Co-Registration and Quantification of τ

To calculate the differences in [^{18}F]-AV1451 uptake between AD and CN, we co-registered the PET images of each subject to the corresponding MRI structural image using PETSurfer (https://surfer.nmr.mgh.harvard.edu/fswiki/PetSurfer, accessed on 24 November 2024). Once the PET images were aligned in the same space as the structural image, since the ROIs' parcellization was in the latter space, we could calculate the τ concentration in each of the 83 ROIs. To have an absolute quantification of each subject, we normalized the concentration values to the cerebellum value (i.e., we divided the concentration values of each brain region by the concentration value in the cerebellum).

Indeed, the cerebellum is known to not be affected by the pathological accumulation of τ protein and it is considered a reference region for [^{18}F-AV1451 metabolism].

4.6. Statistical Analysis

Firstly, the normality and homogeneity of variances of the distributions of τ concentrations for each group (AD and CN) were tested using the Shapiro–Wilks and Levene's tests. This procedure was needed to test the hypothesis of whether the distributions of τ concentrations for AD and CN were those of normal random variables. Then, the difference of [^{18}F]-AV1451 PET uptake between AD and CN was calculated by a Mann–Whitney–Wilcoxon test. The null hypothesis (i.e., AD and CN's tau concentration values belong to the same distribution) was rejected when p-values were below 0.05. In these cases, the post hoc test, Tukey's HSD test, was employed since it is considered robust even when data are unbalanced [44]. Post hoc tests control the family-wise error rate by the Benjamini–Hochberg step-up procedure [45]. The ROIs for which the null hypothesis was rejected were considered significantly different between AD and CN. Significant ROIs were ordered from the most significantly different between AD and CN to the less significant until the non-significant ROIs and the corresponding value of [^{18}F]-AV1451 concentration was considered. In Figure 1, we depict the 83 cortical and subcortical nodes of the brain with colors corresponding to different τ concentrations. For the statistical analysis, we used Python libraries.

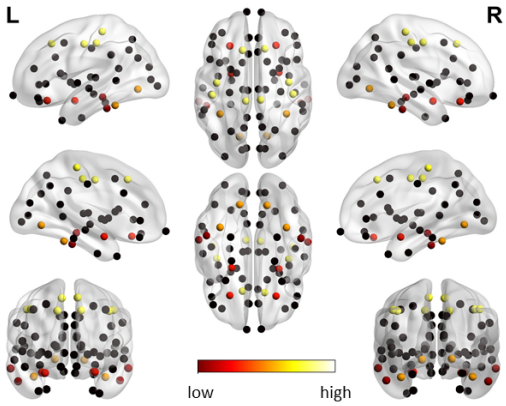

Figure 1. Nodes of the 83 cortical and subcortical ROIs of the brain. The color defines the nodes in which the concentration of τ is significantly greater in AD with respect to CN. The color code defines the increasing order in τ concentration.

5. Results

This section presents the results of the numerical simulations of the four mathematical models corresponding to the different choices for the operator K governing τ spreading. All simulations were conducted using Matlab R2021a on an Intel Core i5 processor with 2.50 GHZ and a Windows operating system. The codes used for the current experiments can be made available upon request to the authors.

5.1. Experimental Setting

The differential system (9) was numerically solved by using the Matlab function `ode45` implementing the Dormand–Prince 5(4) Runge–Kutta method with a variable time step for efficient computation [46]. Since misfolded τ protein has been shown to originate in the entorhinal region of the brain, the source term $s_{\mathbf{w}}(t)$ was chosen as non-null and equal to one only on those vertices belonging to the entorhinal region, i.e., for all $t > 0$, we have

$$(s_{\mathbf{w}}(t))_j = \begin{cases} 1 & j \in \text{ entorhinal region} \\ 0 & \text{otherwise} \end{cases} \tag{21}$$

where $(s_{\mathbf{w}}(t))_j$ denotes the jth component of $s_{\mathbf{w}}(t)$. The seeding region for misfolded τ is shown in Figure 2.

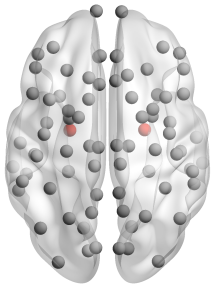

Figure 2. Nodes of the 83 ROIs corresponding to the cortical and subcortical regions of the brain. Colored nodes correspond to the enthorinal regions.

The differential system was integrated from the initial time $t_0 = 0$ to the final time $t_f = 150$. The final time was chosen to correspond to the stabilization of the solutions. In the numerical simulations of the four models, we fixed the values of all parameters of system (9), except γ_3, as reported in Table 1. These values were chosen, on the basis of different tests, as the ones giving the best approach to asymptotic equilibrium in a pathological situation.

Table 1. Fixed parameter values for system (9).

γ_1	γ_2	α	$C_{\mathbf{u}_1}$	$C_{\mathbf{w}}$	σ_1	σ_2	σ_3	σ_4
0.001	0.001	0.12	0.1	0.5	0.1	0.1	0.1	0.11

Moreover, we fixed, for the four models, with the same criterion as above, the parameters reported in Table 2. The procedure used for identifying, for each model, a good γ_3 value will be described in the following subsection.

Table 2. Fixed parameter values for the four models.

$R_{\mathbf{p}}$	δ	$\widetilde{\delta}$	η
25	30	15	5

5.2. Identification of the Parameter γ_3

The statistical analysis described in Section 4.6 shows that the distribution of ^{18}F-AV1451 uptake is not normal for all ROIs. Subsequently, the non-parametric Mann–Whitney–Wilcoxon Test with a Bonferroni correction for multiple comparisons showed that 29 ROIs significantly differ between AD and CN. Table 3 shows the six ROIs, which are mostly different (p-value $< 10^{-5}$) and their respective averaged τ concentrations.

Table 3. p-value and τ concentration (mean $\pm$ st.dev.) in AD and CN for the six most significant ROIs.

ROI	Significance	AD τ Concentration	CN τ Concentration
Fusiform region	8.3×10^{-9}	1.6 ± 0.3	1.2 ± 0.1
Inferior temporal region	1.6×10^{-8}	1.7 ± 0.5	1.2 ± 0.2
Middle temporal region	2.9×10^{-6}	1.6 ± 0.5	1.2 ± 0.2
Lingual region	3.1×10^{-6}	1.4 ± 0.3	1.1 ± 0.1
Lateral orbitofrontal region	5.4×10^{-6}	1.5 ± 0.4	1.2 ± 0.2
Amygdala	6.5×10^{-6}	1.4 ± 0.3	1.2 ± 0.1

The most significant ROIs for the accumulation of τ in AD with respect to CN are, in decreasing order, the inferior temporal region, the fusiform region, the middle temporal region, the lateral orbitofrontal region, the amygdala, and the lingual region. These six regions belong to three different networks (see Appendix A): the inferior temporal and middle temporal regions belong to the temporal network, the fusiform and the lingual regions are part of the occipital network, and the lateral orbitofrontal region and the amygdala are included in the limbic network. Since the brain is organized in several functional discrete networks, as introduced in Section 4, it is convenient to refer to the networks to which these regions belong rather than to the single ROIs. For this reason, we average the values of τ protein in the significant regions belonging to the same network. Let $w_{\mathrm{T}}^{(*)}$ be the average of the τ values obtained from clinical data in the inferior temporal and middle temporal regions. Analogously, let $w_{\mathrm{O}}^{(*)}$ be the mean τ value in the fusiform and the lingual regions and let $w_{\mathrm{L}}^{(*)}$ be the mean τ value in the latter orbital and the amygdala regions.

To evaluate the results obtained from four models, we also considered the value of the τ protein in the sensorimotor network that is known not to be characterized by the pathological accumulation of τ in AD. A good model for AD progression should, in fact, describe the evolution of τ both in the brain areas affected by the disease and in those that are not influenced. Therefore, let $w_{\mathrm{S}}^{(*)}$ be the average τ value in the paracentral, postcentral, precentral, and superior frontal regions forming the sensorimotor network. The τ mean values obtained from clinical data constitute our benchmark; they are ordered in decreasing order as follows:

$$w_{\mathrm{T}}^{(*)} > w_{\mathrm{L}}^{(*)} > w_{\mathrm{O}}^{(*)} > w_{\mathrm{S}}^{(*)}$$

resulting in the string

$$s^{(*)} = \text{“TLOS”}$$

which, therefore, represents the decreasing order of τ values in clinical data. Brain regions with a higher concentration of misfolded τ are more deteriorated; therefore, $s^{(*)}$ represents a *clinical deterioration pattern* of a brain with AD. We stress that this deterioration pattern considers only the brain regions that are significative for AD, according to our statistical analysis. Mathematical models should reproduce, in the best possible way, this deterioration pattern to be reliable tools for the analysis of AD progression. We remark that our benchmark TLOS is consistent with the literature and with the Braak stages, considering that the temporal and limbic regions are mostly affected, even in the early stages (Stages I and II) and central stages (in particular, the amygdala is involved in Stage IV), while, only in the latest stage (Stage VI), is there a final involvement of the motor and sensory areas, which corresponds to the fact that, in our data, the sensorimotor regions have low tau concentrations values. The parieto-occipital involvement has been demonstrated in more recent literature as being correlated with visuospatial dysfunction, especially in the early stage of the disease [47].

To evaluate the ability of the models to reproduce the deterioration pattern, we considered, for each model j, $j = 1, \ldots, 4$, the values of τ protein at the final time t_f. We averaged the values on the vertices belonging to the inferior temporal and middle temporal regions to obtain $w_{\mathrm{T}}^{(j)}$, $j = 1, \ldots, 4$. Proceeding similarly, we obtained $w_{\mathrm{L}}^{(j)}$, $w_{\mathrm{O}}^{(j)}$, and $w_{\mathrm{S}}^{(j)}$ as mean τ values on the vertices belonging to the later orbital and the amygdala regions, the fusiform and the lingual regions and the paracentral, postcentral, precentral, and superior frontal regions, respectively. For each model j, we defined the string $s^{(j)}$ formed using the letters T, L, O, and S sorted in decreasing order of τ values $w_{\mathrm{T}}^{(j)}$, $w_{\mathrm{L}}^{(j)}$, $w_{\mathrm{O}}^{(j)}$, and $w_{\mathrm{S}}^{(j)}$. We used the Hamming distance (HD) between the strings $s^{(*)}$ and $s^{(j)}$, $j = 1, \ldots, 4$ to measure the distance between the clinical and the models' deterioration patterns. We recall that the Hamming distance between two strings is the number of positions at which the two strings differ [48]. The value of the parameter γ_3 was experimentally determined by trial and error to identify, for each model, the best outcome in terms of Hamming distance. Since, for each

model, intervals of values exist for γ_3 giving the same optimal Hamming distance value, we identified the best γ_3 value in such intervals as follows. We define the vector

$$\mathbf{w}^{(*)} = (\tilde{w}_{\mathrm{T}}^{(*)}, \tilde{w}_{\mathrm{L}}^{(*)}, \tilde{w}_{\mathrm{O}}^{(*)}, \tilde{w}_{\mathrm{S}}^{(*)})^T$$

whose components, which are normalized τ values ranging from 0 to 1, are defined as follows:

$$\tilde{w}_{\mathrm{T}}^{(*)} = \frac{w_{\mathrm{T}}^{(*)}}{w_{\mathrm{T}}^{(*)}},\ \tilde{w}_{\mathrm{L}}^{(*)} = \frac{w_{\mathrm{L}}^{(*)}}{w_{\mathrm{T}}^{(*)}},\ \tilde{w}_{\mathrm{O}}^{(*)} = \frac{w_{\mathrm{O}}^{(*)}}{w_{\mathrm{T}}^{(*)}},\ \tilde{w}_{\mathrm{S}}^{(*)} = \frac{w_{\mathrm{S}}^{(*)}}{w_{\mathrm{T}}^{(*)}}.$$

Then, we define the vectors

$$\mathbf{w}^{(j)} = (\tilde{w}_{\mathrm{T}}^{(j)}, \tilde{w}_{\mathrm{L}}^{(j)}, \tilde{w}_{\mathrm{O}}^{(j)}, \tilde{w}_{\mathrm{S}}^{(j)})^T,$$

where

$$\tilde{w}_{\mathrm{T}}^{(j)} = \frac{w_{\mathrm{T}}^{(j)}}{M^{(j)}},\ \tilde{w}_{\mathrm{L}}^{(j)} = \frac{w_{\mathrm{L}}^{(j)}}{M^{(j)}},\ \tilde{w}_{\mathrm{O}}^{(j)} = \frac{w_{\mathrm{O}}^{(j)}}{M^{(j)}},\ \tilde{w}_{\mathrm{S}}^{(j)} = \frac{w_{\mathrm{S}}^{(j)}}{M^{(j)}},$$

and $M^{(j)} = \max\{w_{\mathrm{T}}^{(j)}, w_{\mathrm{L}}^{(j)}, w_{\mathrm{O}}^{(j)}, w_{\mathrm{S}}^{(j)}\}$ for $j = 1, \ldots, 4$. As a measure of the distance between $\mathbf{w}^{(*)}$ and $\mathbf{w}^{(j)}$, we can use the Root Mean Square Error (RMSE) and the Mean Absolute Error (MAE). We recall that, given a computed vector $\mathbf{w} \in \mathbb{R}^4$ of τ values, these error measures are , respectively, defined as

$$\mathrm{RMSE} = \sqrt{\frac{\|\mathbf{w}^{(*)} - \mathbf{w}\|_2^2}{4}},$$

$$\mathrm{MAE} = \frac{\|\mathbf{w}^{(*)} - \mathbf{w}\|_1}{4}$$

where $\|\cdot\|_2$ and $\|\cdot\|_2$ denote the L_2 and L_1 norms. Among all the γ_3 values corresponding to the same optimal HD value, we heuristically determine the value that achieves the best RMSE reduction. This leads to four values for γ_3, one for each model, shown in Table 4. We observe that the identified optimal γ_3 value is the same for Model 1 and Model 2.

Table 4. Identified optimal values for γ_3.

Model 1	**Model 2**	**Model 3**	**Model 4**
0.001	0.001	150	0.05

5.3. Numerical Results

Table 5 shows the clinical and computed deterioration patterns; Table 6 reports the corresponding HD, RMSE, and MAE values.

Table 5. Clinical and models' deterioration patterns.

Clinical Data	**Model 1**	**Model 2**	**Model 3**	**Model 4**
T	L	T	L	L
L	T	L	S	S
O	O	O	T	O
S	S	S	O	T

Table 6. Numerical results for the four models.

	Model 1	**Model 2**	**Model 3**	**Model 4**
HD	2	0	4	3
RMSE	0.11574	0.11543	0.10931	0.10615
MAE	0.09256	0.09212	0.08911	0.08950

In Figure 3, we show the deterioration pattern in the significative brain regions from clinical data and from the four different models.

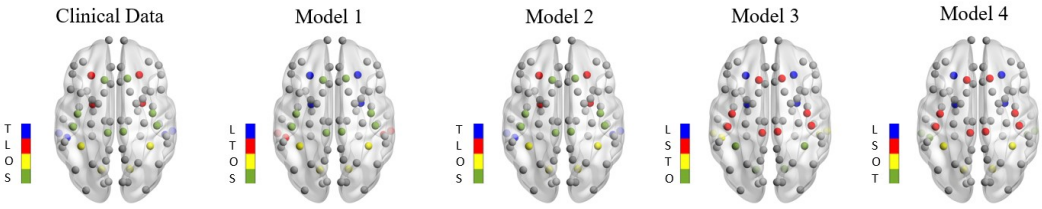

Figure 3. Deterioration pattern in the significative brain regions. From left to right: clinical data, Model 1, Model 2, Model 3, and Model 4. The non-significative regions are displayed in gray. In the color bar, the colors correspond to decreasing τ values in the significative regions.

From the results shown above, it is clear that the only model capable of reproducing the clinical deterioration pattern is Model 2. A diffusion operator along the cumulative connectome seems to be the most appropriate operator for modeling the spreading of τ protein in a brain with AD. Model 1 uses a diffusion operator too, but, comparing the deterioration patterns of Model 1 and Model 2, it is evident that the cumulative connectome, encoding information on brain regions connected along long distances, is a key tool. Even if Model 1 does not exactly reproduce the clinical deterioration pattern, it is able to distinguish between deteriorated and non-deteriorated regions, since the letter S is in the last position in the string $w^{(1)}$, as it should be. We observe from Table 6 that models 3 and 4 give the best results in terms of RMSE and MAE reduction. However, they do not reproduce the deterioration pattern of AD and do not distinguish between deteriorated and non-deteriorated regions (the letter S is in the second position both in $w^{(3)}$ and $w^{(4)}$). For this reason, they do not seem to be good models for the spreading of misfolded τ in presence of AD.

6. Discussion

In this study, we had two main objectives. We were interested in (1) comparing different modeling possibilities concerning the spreading of τ protein in a brain with AD, when the $A\beta$ protein is also present and the synergy between the two was considered; (2) producing clinical data that can be compared with the outputs of the models in order to verify their reliability. We believe that the lack of comparison between the results of a theoretical model and clinical data could be considered a deficiency that should be rectified in order to support the usefulness of mathematical models in AD [49]. To this end, we evolved the two proteins on appropriate networks, created from the medical data of human connectomes. The need for different connectomes was dictated by both the physiology of the brain and the biological characteristics of the proteins themselves. We therefore considered, for the evolution of $A\beta$, which travels only on short distances, an intrinsic proximity connectome, and a standard diffusion Laplacian on it. With regard to τ spreading, which is supposed to possibly travel with a prion-like mechanism and over long distances, we considered four distinct mathematical models on as many networks: a diffusion via Laplacian on a structural connectome and on a cumulative connectome, and a spreading via convolution on two further different connectomes. We emphasize that the so-called intrinsic proximity connectome and the cumulative connectome were introduced in this work for the first time. We identified from public multimodal data, with a careful statistical

analysis, six regions relevant when it comes to AD and we evaluated τ concentrations in them, obtaining a degradation pattern that was crucial for us to verify the goodness of the models.

By comparing the results of the simulations with clinical data, we saw that only the model using the cumulative connectome was able to correctly reproduce the clinical degradation pattern, which also includes a network that is not damaged by the disease. We hypothesize that this result is due to the fact that the cumulative connectome encodes information on brain regions connected along long distances. On the basis of these findings, we feel that we can say that the models are not all equivalent, and that the comparison with clinical data is a crucial element to be able to assess their reliability. Of course, the results obtained here relate to the specific case of AD, and it is plausible that, for other diseases, the same models give different performances. As a next step, we are going to apply the same paradigm of analysis, i.e., a close comparison with appropriate clinical data, to the models enriched by taking into account atrophy, to be more realistic and see if something relevant happens. We believe that a highly interdisciplinary study, such as the one reported in the paper, could be a very promising direction in which cutting-edge biomedical mathematical research could be heading.

Author Contributions: All authors have contributed equally to this work. All authors have read and agreed to the published version of the manuscript.

Funding: This research was supported by the AlmaIdea 2022 programme of the Alma Mater Studiorum—Università di Bologna, project n. CUPJ45F21002000001.

Institutional Review Board Statement: As per ADNI protocols, all procedures performed in studies involving human participants were in accordance with the ethical standards of the institutional and/or national research committee and with the 1964 Helsinki declaration and its later amendments or comparable ethical standards. More details can be found at adni.loni.usc.edu. (This article does not contain any studies with human participants performed by any of the authors)

Informed Consent Statement: Authors received the consent for publication from ADNI.

Data Availability Statement: Publicly available datasets were analyzed in this study. These data can be found at the following urls: http://adni.loni.usc.edu and https://braingraph.org (accessed on 24 November 2024); see [14,15]. All data produced by the authors are available upon request from the authors.

Acknowledgments: Data collection and sharing for this project was funded by the Alzheimer's Disease Neuroimaging Initiative (ADNI) (National Institutes of Health Grant U01 AG024904) and DOD ADNI (Department of Defense award number W81XWH-12-2-0012). ADNI is funded by the National Institute on Aging, the National Institute of Biomedical Imaging and Bioengineering, and through generous contributions from the following: AbbVie, Alzheimer's Association; Alzheimer's Drug Discovery Foundation; Araclon Biotech; BioClinica, Inc.; Biogen; Bristol-Myers Squibb Company; CereSpir, Inc.; Cogstate; Eisai Inc.; Elan Pharmaceuticals, Inc.; Eli Lilly and Company; EuroImmun; F. Hoffmann-La Roche Ltd. and its affiliated company Genentech, Inc.; Fujirebio; GE Healthcare; IXICO Ltd.; Janssen Alzheimer Immunotherapy Research & Development, LLC.; Johnson & Johnson Pharmaceutical Research & Development LLC.; Lumosity; Lundbeck; Merck & Co., Inc.; Meso Scale Diagnostics, LLC.; NeuroRx Research; Neurotrack Technologies; Novartis Pharmaceuticals Corporation; Pfizer Inc.; Piramal Imaging; Servier; Takeda Pharmaceutical Company; and Transition Therapeutics. The Canadian Institutes of Health Research is providing funds to support ADNI clinical sites in Canada. Private sector contributions are facilitated by the Foundation for the National Institutes of Health (www.fnih.org). The grantee organization is the Northern California Institute for Research and Education, and the study is coordinated by the Alzheimer's Therapeutic Research Institute at the University of Southern California. ADNI data are disseminated by the Laboratory for Neuro Imaging at the University of Southern California.

Conflicts of Interest: The authors declare no conflicts of interest.

Appendix A

Table A1. List of anatomical cortical and subcortical ROIs identified with FreeSurfer, and the six networks: frontal, occipital, temporal, limbic, sensorimotor network, and basal ganglia.

Region of Interest	Network
Nucleus accumbens	Limbic
Amygdala	Limbic
Bankssts	Temporal
Brain Stem	Limbic
Caudal anterior cingulate gyrus	Limbic
Caudal middle frontal gyrus	Frontal
Caudate	Basal ganglia
Cuneus	Occipital
Entorhinal gyrus	Limbic
Frontal pole	Frontal
Fusiform gyrus	Occipital
Hippocampus	Limbic
Inferior parietal gyrus	Parietal
Inferior temporal gyrus	Temporal
Insula	Limbic
Isthmus cingulate gyrus	Limbic
Lateral occipital gyrus	Occipital
Lateral orbito frontal gyrus	Limbic
Lingual gyrus	Occipital
Medial orbito frontal gyrus	Limbic
Middle temporal gyrus	Temporal
Pallidum	Basal ganglia
Paracentral gyrus	Sensorimotor
Parahippocampal gyrus	Limbic
Pars opercularis	Frontal
Pars orbitalis	Frontal
Pars triangularis	Frontal
Peri calcarine gyrus	Occipital
Postcentral gyrus	Sensorimotor
Posterior cingulate gyrus	Limbic
Precentral gyrus	Sensorimotor
Precuneus	Parietal
Putamen	Basal ganglia
Rostral anterior cingulate gyrus	Limbic
Rostral middle frontal gyrus	Frontal
Superior frontal gyrus	Sensorimotor
Superior parietal gyrus	Parietal
Superior temporal gyrus	Temporal
Supramarginal gyrus	Parietal
Temporal pole	Temporal
Transverse temporal gyrus	Temporal

References

1. Ossenkoppele, R.; Rabinovici, G.D.; Smith, R.; Cho, H.; Schöll, M.; Strandberg, O.; Palmqvist, S.; Mattsson, N.; Janelidze, S.; Santillo, A.; et al. Discriminative accuracy of [18F] flortaucipir positron emission tomography for Alzheimer disease vs. other neurodegenerative disorders. *JAMA* **2018**, *320*, 1151–1162. [CrossRef] [PubMed]
2. Braak, H.; Braak, E. Neuropathological stageing of Alzheimer-related changes. *Acta Neuropathol.* **1991**, *82*, 239–259. [CrossRef]
3. Grothe, M.J.; Barthel, H.; Sepulcre, J.; Dyrba, M.; Sabri, O.; Teipel, S.J.; Initiative, A.D.N.; Initiative, A.D.N. In vivo staging of regional amyloid deposition. *Neurology* **2017**, *89*, 2031–2038. [CrossRef]
4. Busche, M.A.; Hyman, B.T. Synergy between amyloid-β and tau in Alzheimer's disease. *Nat. Neurosci.* **2020**, *23*, 1183–1193. [CrossRef]
5. Thompson, T.B.; Chaggar, P.; Kuhl, E.; Goriely, A.; Initiative, A.D.N. Protein-protein interactions in neurodegenerative diseases: A conspiracy theory. *PLoS Comput. Biol.* **2020**, *16*, e1008267. [CrossRef] [PubMed]

6. Bertsch, M.; Franchi, B.; Raj, A.; Tesi, M.C. Macroscopic modelling of Alzheimer's disease: Difficulties and challenges. *Brain Multiphys.* **2021**, *2*, 100040. [CrossRef]
7. Kim, J.; Jeong, M.; Stiles, W.R.; Choi, H.S. Neuroimaging modalities in Alzheimer's disease: Diagnosis and clinical features. *Int. J. Mol. Sci.* **2022**, *23*, 6079. [CrossRef]
8. Bassett, D.S.; Bullmore, E.T. Human brain networks in health and disease. *Curr. Opin. Neurol.* **2009**, *22*, 340–347. [CrossRef]
9. Sporns, O.; Zwi, J.D. The small world of the cerebral cortex. *Neuroinformatics* **2004**, *2*, 145–162. [CrossRef]
10. Torok, J.; Anand, C.; Verma, P.; Raj, A. Connectome-based biophysics models of Alzheimer's disease diagnosis and prognosis. *Transl. Res.* **2023**, *254*, 13–23. [CrossRef]
11. Bertsch, M.; Franchi, B.; Tesi, M.C.; Tora, V. The role of A β and Tau proteins in Alzheimer's disease: A mathematical model on graphs. *J. Math. Biol.* **2023**, *87*, 49. [CrossRef] [PubMed]
12. Catani, M.; Mesulam, M. What is a disconnection syndrome? *Cortex* **2008**, *44*, 911–913. [CrossRef]
13. Mesulam, M.M. A cortical network for directed attention and unilateral neglect. *Ann. Neurol. Off. J. Am. Neurol. Assoc. Child Neurol. Soc.* **1981**, *10*, 309–325. [CrossRef] [PubMed]
14. Szalkai, B.; Kerepesi, C.; Varga, B.; Grolmusz, V. High-resolution directed human connectomes and the consensus connectome dynamics. *PLoS ONE* **2019**, *14*, e0215473. [CrossRef] [PubMed]
15. Szalkai, B.; Kerepesi, C.; Varga, B.; Grolmusz, V. Parameterizable consensus connectomes from the human connectome project: The budapest reference connectome server v3. 0. *Cogn. Neurodyn.* **2017**, *11*, 113–116. [CrossRef] [PubMed]
16. Grigor'yan, A. *Introduction to Analysis on Graphs*; American Mathematical Society: Providence, RI, USA, 2018; Volume 71.
17. McNab, J.A.; Edlow, B.L.; Witzel, T.; Huang, S.Y.; Bhat, H.; Heberlein, K.; Feiweier, T.; Liu, K.; Keil, B.; Cohen-Adad, J.; et al. The Human Connectome Project and beyond: Initial applications of 300 mT/m gradients. *Neuroimage* **2013**, *80*, 234–245. [CrossRef]
18. Giuffrida, M.L.; Caraci, F.; Pignataro, B.; Cataldo, S.; De Bona, P.; Bruno, V.; Molinaro, G.; Pappalardo, G.; Messina, A.; Palmigiano, A.; et al. β-amyloid monomers are neuroprotective. *J. Neurosci.* **2009**, *29*, 10582–10587. [CrossRef]
19. Haass, C.; Selkoe, D.J. Soluble protein oligomers in neurodegeneration: Lessons from the Alzheimer's amyloid β-peptide. *Nat. Rev. Mol. Cell Biol.* **2007**, *8*, 101–112. [CrossRef]
20. Ono, K.; Condron, M.M.; Teplow, D.B. Structure–neurotoxicity relationships of amyloid β-protein oligomers. *Proc. Natl. Acad. Sci. USA* **2009**, *106*, 14745–14750. [CrossRef]
21. Meyer-Luehmann, M.; Spires-Jones, T.L.; Prada, C.; Garcia-Alloza, M.; De Calignon, A.; Rozkalne, A.; Koenigsknecht-Talboo, J.; Holtzman, D.M.; Bacskai, B.J.; Hyman, B.T. Rapid appearance and local toxicity of amyloid-β plaques in a mouse model of Alzheimer's disease. *Nature* **2008**, *451*, 720–724. [CrossRef]
22. Grundke-Iqbal, I.; Iqbal, K.; Tung, Y.; Quinlan, M.; Wisniewski, H.; Binder, L. Abnormal phosphorylation of the microtubule-associated protein τ (tau) in Alzheimer cytoskeletal pathology. *Alzheimer Dis. Assoc. Disord.* **1987**, *1*, 202. [CrossRef]
23. Ittner, L.M.; Götz, J. Amyloid-β and tau—A toxic pas de deux in Alzheimer's disease. *Nat. Rev. Neurosci.* **2011**, *12*, 67–72. [CrossRef] [PubMed]
24. Ricciarelli, R.; Fedele, E. The amyloid cascade hypothesis in Alzheimer's disease: It's time to change our mind. *Curr. Neuropharmacol.* **2017**, *15*, 926–935. [CrossRef]
25. Bloom, G.S. Amyloid-β and tau: The trigger and bullet in Alzheimer disease pathogenesis. *JAMA Neurol.* **2014**, *71*, 505–508. [CrossRef]
26. Bennett, R.E.; DeVos, S.L.; Dujardin, S.; Corjuc, B.; Gor, R.; Gonzalez, J.; Roe, A.D.; Frosch, M.P.; Pitstick, R.; Carlson, G.A.; et al. Enhanced tau aggregation in the presence of amyloid β. *Am. J. Pathol.* **2017**, *187*, 1601–1612. [CrossRef]
27. Small, S.A.; Duff, K. Linking Aβ and tau in late-onset Alzheimer's disease: A dual pathway hypothesis. *Neuron* **2008**, *60*, 534–542. [CrossRef]
28. Braak, H.; Del Tredici, K. Alzheimer's pathogenesis: Is there neuron-to-neuron propagation? *Acta Neuropathol.* **2011**, *121*, 589–595. [CrossRef] [PubMed]
29. Goedert, M.; Spillantini, M.G. Propagation of Tau aggregates. *Mol. Brain* **2017**, *10*, 18. [CrossRef]
30. Tatarnikova, O.; Orlov, M.; Bobkova, N. Beta-amyloid and tau-protein: Structure, interaction, and prion-like properties. *Biochemistry* **2015**, *80*, 1800–1819. [CrossRef]
31. Dujardin, S.; Hyman, B.T. Tau prion-like propagation: State of the art and current challenges. In *Tau Biology*; Takashima, A., Wolozin, B., Buee, L., Eds.; Springer: Singapore, 2020; pp. 305–325.
32. Ahmed, Z.; Cooper, J.; Murray, T.K.; Garn, K.; McNaughton, E.; Clarke, H.; Parhizkar, S.; Ward, M.A.; Cavallini, A.; Jackson, S.; et al. A novel in vivo model of tau propagation with rapid and progressive neurofibrillary tangle pathology: The pattern of spread is determined by connectivity, not proximity. *Acta Neuropathol.* **2014**, *127*, 667–683. [CrossRef] [PubMed]
33. Raj, A.; Kuceyeski, A.; Weiner, M. A network diffusion model of disease progression in dementia. *Neuron* **2012**, *73*, 1204–1215. [CrossRef] [PubMed]
34. Raj, A.; Tora, V.; Gao, X.; Cho, H.; Choi, J.Y.; Ryu, Y.H.; Lyoo, C.H.; Franchi, B. Combined model of aggregation and network diffusion recapitulates Alzheimer's regional tau-positron emission tomography. *Brain Connect.* **2021**, *11*, 624–638. [CrossRef] [PubMed]
35. Raj, A. Graph models of pathology spread in Alzheimer's disease: An alternative to conventional graph theoretic analysis. *Brain Connect.* **2021**, *11*, 799–814. [CrossRef] [PubMed]

36. Pal, S.; Melnik, R. Nonlocal multiscale interactions in brain neurodegenerative protein dynamics and coupled proteopathic processes. In Proceedings of the 9th Edition of the International Conference on Computational Methods for Coupled Problems in Science and Engineering (Coupled Problems 2021), Online Event, 13–16 June 2021; pp. 14–16.
37. Pal, S.; Melnik, R. Nonlocal models in the analysis of brain neurodegenerative protein dynamics with application to Alzheimer's disease. *Sci. Rep.* **2022**, *12*, 7328. [CrossRef]
38. Fornari, S.; Schäfer, A.; Jucker, M.; Goriely, A.; Kuhl, E. Prion-like spreading of Alzheimer's disease within the brain's connectome. *J. R. Soc. Interface* **2019**, *16*, 20190356. [CrossRef]
39. Fornari, S.; Schäfer, A.; Kuhl, E.; Goriely, A. Spatially-extended nucleation-aggregation-fragmentation models for the dynamics of prion-like neurodegenerative protein-spreading in the brain and its connectome. *J. Theor. Biol.* **2020**, *486*, 110102. [CrossRef]
40. Goriely, A.; Kuhl, E.; Bick, C. Neuronal oscillations on evolving networks: Dynamics, damage, degradation, decline, dementia, and death. *Phys. Rev. Lett.* **2020**, *125*, 128102. [CrossRef]
41. Shuman, D.I.; Narang, S.K.; Frossard, P.; Ortega, A.; Vandergheynst, P. The emerging field of signal processing on graphs: Extending high-dimensional data analysis to networks and other irregular domains. *IEEE Signal Process. Mag.* **2013**, *30*, 83–98. [CrossRef]
42. Evangelisti, S.; Testa, C.; Ferri, L.; Gramegna, L.L.; Manners, D.N.; Rizzo, G.; Remondini, D.; Castellani, G.; Naldi, I.; Bisulli, F.; et al. Brain functional connectivity in sleep-related hypermotor epilepsy. *NeuroImage Clin.* **2018**, *17*, 873–881. [CrossRef]
43. Mesulam, M.M. From sensation to cognition. *Brain A J. Neurol.* **1998**, *121*, 1013–1052. [CrossRef]
44. Brown, A.M. A new software for carrying out one-way ANOVA post hoc tests. *Comput. Methods Programs Biomed.* **2005**, *79*, 89–95. [CrossRef] [PubMed]
45. Benjamini, Y.; Hochberg, Y. Controlling the false discovery rate: A practical and powerful approach to multiple testing. *J. R. Stat. Soc. Ser. B (Methodol.)* **1995**, *57*, 289–300. [CrossRef]
46. Dormand, J.R.; Prince, P.J. A family of embedded Runge–Kutta formulae. *J. Comput. Appl. Math.* **1980**, *6*, 19–26. [CrossRef]
47. Cho, H.; Choi, J.Y.; Lee, S.H.; Lee, J.H.; Choi, Y.C.; Ryu, Y.H.; Lee, M.S.; Lyoo, C.H. Excessive tau accumulation in the parieto-occipital cortex characterizes early-onset Alzheimer's disease. *Neurobiol. Aging* **2017**, *53*, 103–111. [CrossRef] [PubMed]
48. Hutcheson, K. A test for comparing diversities based on Shannon formula. *J. Theor. Biol.* **1970**, *29*, 151–154. [CrossRef]
49. Moravveji, S.; Doyon, N.; Mashreghi, J.; Duchesne, S. A scoping review of mathematical models covering Alzheimer's disease progression. *Front. Neuroinform.* **2024**, *18*, 1281656. [CrossRef] [PubMed]